Chapter 22 – EXPERIMENTAL INVESTIGATIONS ON THE VFE-2 CONFIGURATION AT GLASGOW UNIVERSITY, UNITED KINGDOM

by

Frank N. Coton, Shabudin Bin Mat, Roderick A.McD. Galbraith

22.1 INTRODUCTION

As part of the VFE-2 activities, Glasgow University constructed a replica of the Chu and Luckring [22-1] model for studies in the Glasgow University low speed wind tunnel. The model constructed at Glasgow is physically the largest model in VFE-2 team working project. The model has a root chord length of 1.059 m and a span of 0.987 m. It has an overall thickness of 36 mm. All four of the leading edge geometries were manufactured at Glasgow but, in accordance with the focus of the VFE-2 working group, only results for the sharp and medium radius leading edges will be presented here. In the wind tunnel experiments at Glasgow, a combination of force measurement and flow visualization were used to characterize the flow behavior.

22.2 EXPERIMENTAL SET UP AND WIND TUNNEL TESTING

22.2.1 Wind Tunnel Model

The VFE-2 model is a 65° delta wing with flat upper and lower surfaces (Figure 22-1). In the original paper of Chu and Luckring the entire geometry of the model is specified analytically and this is a major aid to accurate manufacture. The Glasgow University model has a chord length of 1.059 m, giving a wing area of 0.523 m^2. The model was machined from aluminum in five parts; upper surface, lower main body, two leading edges and trailing edge. In all, four sets of leading edges were manufactured ranging from sharp to highly rounded. In the current paper, only results for the sharp and medium radius leading edges sets are presented.

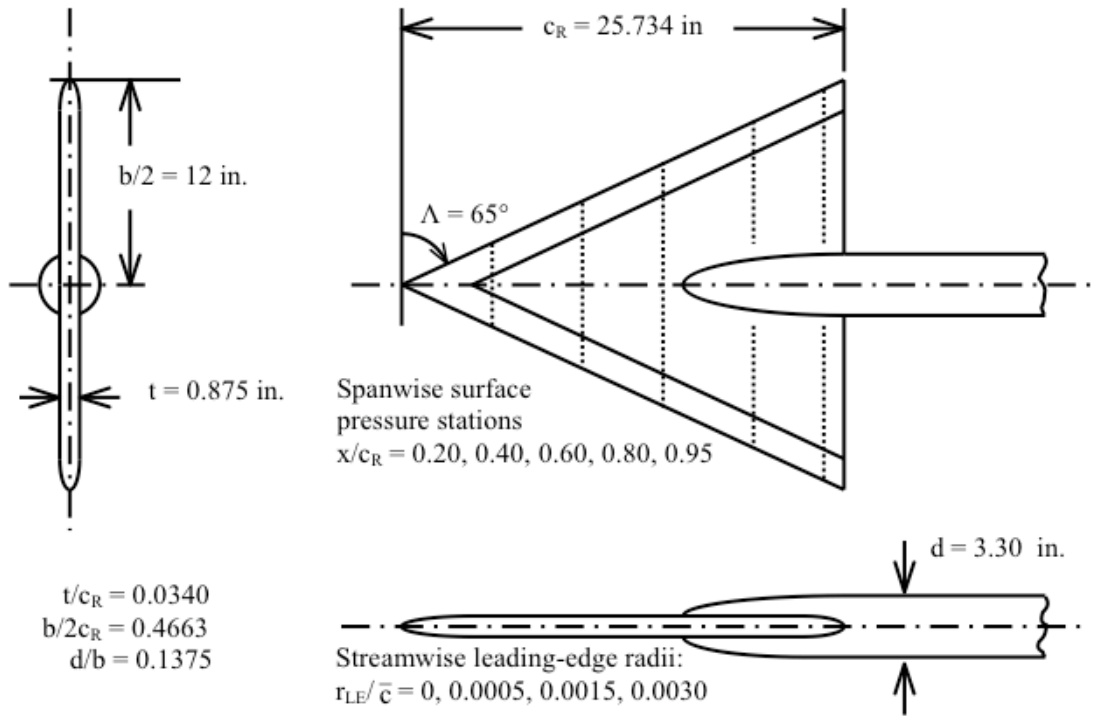

Figure 22-1: Model Geometry (Taken from Ref. [22-1]).

22.2.2 Test Set-up

The wind tunnel test set up involved the model being sting mounted from behind with the sting supported on a fabricated section located two chord lengths downstream of the model. The sting itself consisted of 3 main sub sting components; i.e. short sting, stub-sting and roller housing. The short sting, closest to the model, was set at an angle of 15 degrees to the straight line between the centre of rotation and the mounting point on the support section. This is, in turn, connected at its downstream end to the stub sting which was offset from the straight line between the mounting point and the centre of rotation by 17 degrees. The final part of the sting assembly was the roller housing which provided the interface between the sting and the support section. Its main function was to attach the sting to the support section whilst allowing the sting to move around the section. By moving the roller housing vertically on the support section, the model could be set at an angle of attack of between 0 and 30 degrees, rotating about its centre of rotation at the half root chord point. The general test set-up is shown in Figure 22-2.

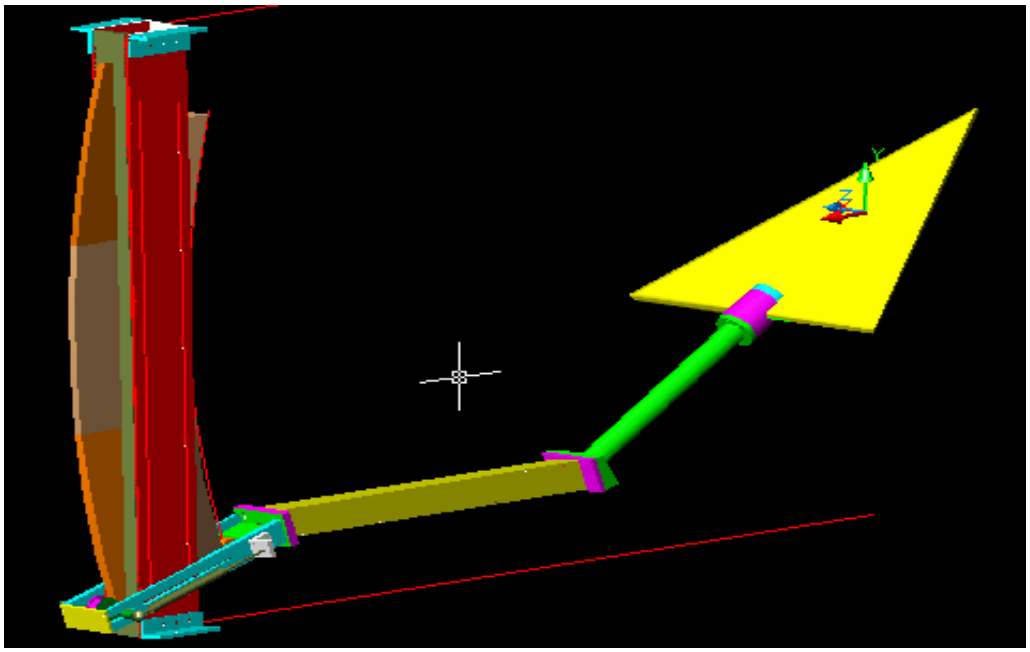

Figure 22-2 (a): Test Set Up.

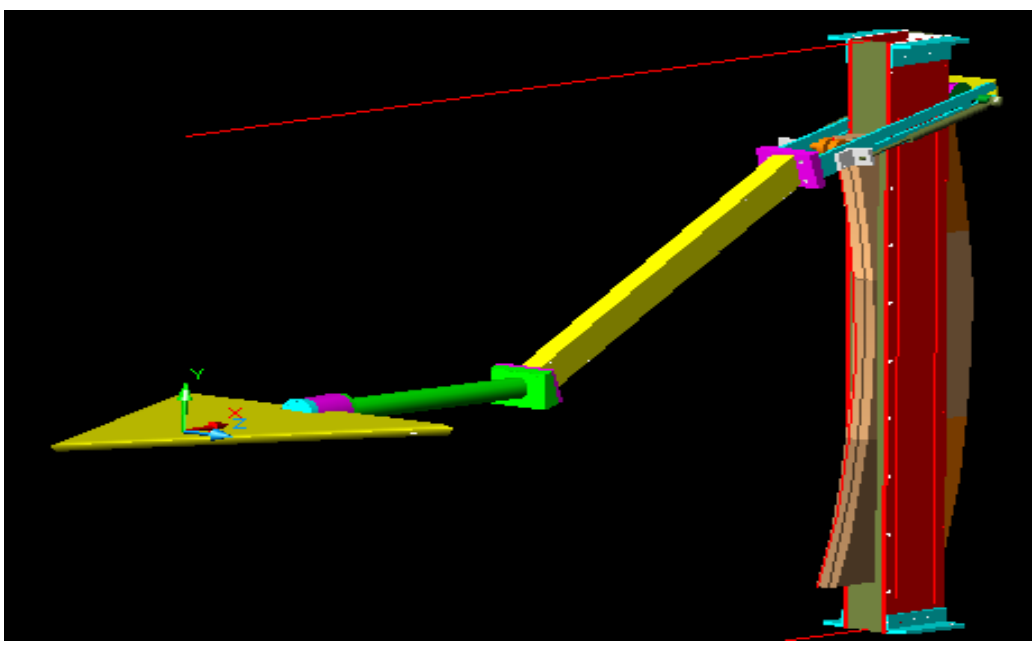

Figure 22-2 (b): Test Set Up (Alternative View).

Carbon fiber fairings for the short sting and wing interface were manufactured according to the analytic descriptions provided by Chu and Luckring to ensure that the entire model/sting geometry replicated the original NASA test. A factory modified six-component AMTI MC5-1250-6 loadcell was located between the

model and the short sting and was used measure the steady and unsteady forces acting on the wing. This loadcell is cylindrical and fitted neatly below the sting fairings and so care was taken to ensure that there was no transmission of load occurred through the fairings. Figure 22-3 shows load cell interface with the model with the short sting fairing covering the non-sensing section of the loadcell. Also shown in this figure is the location on the model of the inclinometer that was used to measure model angle of attack to within 0.05°.

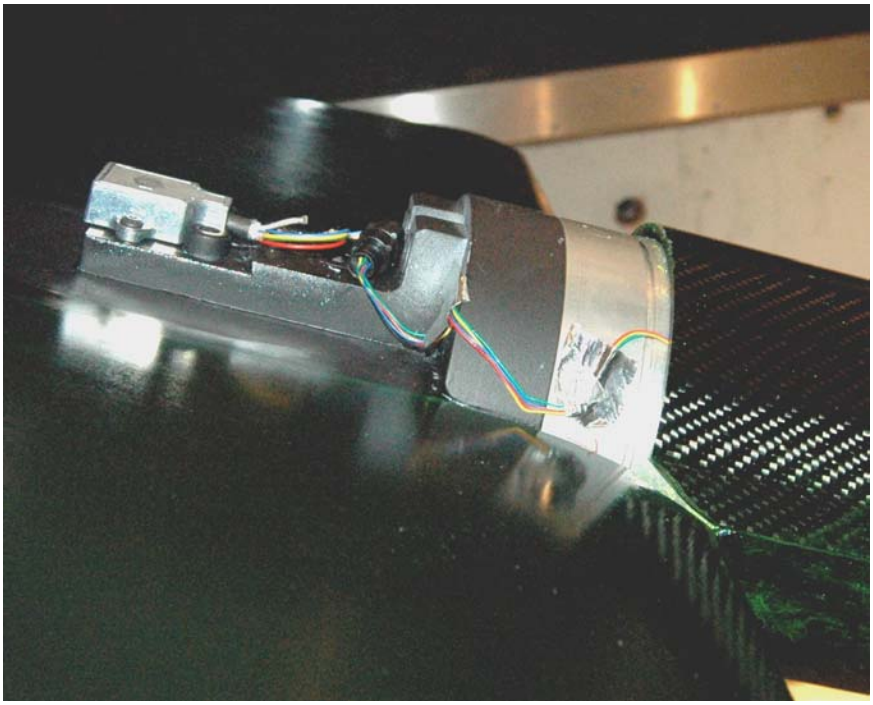

Figure 22-3: Balance and Inclinometer Attachment to the Delta Wing.

The final assembly is shown installed in the wind tunnel in Figure 22-4 where it may also be observed that additional stiffening of the sting assembly is provided by lateral and vertical bracing wires.

Figure 22-4: Model in the Glasgow University Argyll Wind Tunnel.

22.2.3 Wind Tunnel Testing

The experiments were carried out in the 2.65 x 2.04 meter, closed circuit, Argyll Wind Tunnel of the University of Glasgow. Tests were conducted at Reynolds numbers of 1 x 10^6 and 2 x 10^6 based on the mean aerodynamic chord and were conducted in two phases. In the first phase, force and moment data were recorded for the model at each angle of attack. In the second phase, oil flow visualization studies were conducted.

For the forces and moments, measurements were made at each angle of attack at sampling frequencies of 8 kHz and 100 Hz. Each test was repeated five times to determine repeatability. Time averaged values of the forces and moments were calculated from the measured data together with power spectra for each of the force components. In doing this, the natural frequency of the model and support structure was determined a priori and was removed from the spectra by digital filtering.

Oil flow visualization was carried out at 13.3°, 18.5° and 23° angles of attack for both 1 and 2 million Reynolds number. A mixture of Ondina oil thinned with paraffin was mixed with Dayglo powder and applied to the surface of the delta wing. The wind was then turned on and the flow pattern allowed to develop on the surface of the wing. After the flow pattern had stabilized, it was illuminated using ultraviolet light and photographed from above using a digital camera.

22.3 THE DELTA WING FLOWFIELD

22.3.1 Sharp Leading Edge

The flow on a slender delta wing at a certain speed and angle of attack can be described as a movement of the flow from the lower surface to the upper surface in a spiral type of motion. Flow separation will take place

at the leading edge and the resulting shear layer will roll up over the upper surface to form a primary vortex [22-2]. In effect, the primary vortices originate from a series of smaller vortices shed from the leading edge of the wing and contained within the shear layer. They rotate around each other to form the larger primary vortices as shown in Figure 22-5. As the angle of attack is increased the primary vortices grow both in strength and size. As they do so, the axial velocity in the core of the vortex can exceed three times the free stream speed [22-3].

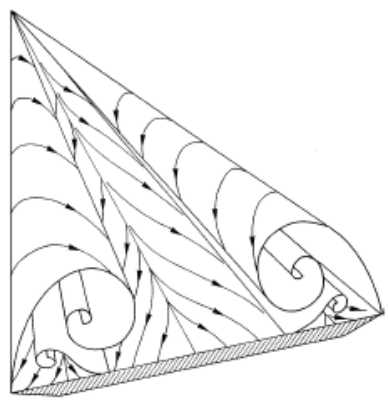

Figure 22-5: Delta Wing Flowfield (Taken from Ref. [22-4]).

Underneath each primary vortex, an attached flow is established on the upper surface of the wing with an attachment line located at a certain span-wise location. Due to the adverse pressure gradient, the attached flow will experience another flow separation which results in the formation of a secondary vortex. The secondary vortex is formed under the primary vortex [22-4]. It is located close to the leading edge but the exact position of the primary attachment and secondary separation lines depends on the angle of attack and Reynolds number. The status of the boundary layer on the wing has a very strong influence on the formation and size of the secondary vortex. The secondary vortex is bigger if the upper surface boundary layer is laminar. This is due to flow separation occurring earlier compared to a turbulent boundary layer. The larger secondary vortex causes a displacement of the primary vortex upwards and inwards [22-3].

At a certain point along the vortex axis, the structure of the primary vortex starts to break down. This happens as a result of the flow suddenly becoming stagnant and turning into an unsteady and unstructured flow. This situation is called vortex breakdown and its location depends on the wing sweep and angle of attack. At moderate angle of attack, vortex breakdown occurs at the trailing edge and moves upstream with increasing angle of attack. Experiments have shown that the breakdown position over a wing can be influenced by the geometry of the wing, tunnel wall interference, support interference, model deformation and Reynolds number [22-5].

22.3.2 Rounded Leading Edge

For a rounded leading edge, the flow separation location is no longer fixed to the leading edge. At a certain angle of attack and speed [[22-6], [22-7]] the primary separation line for the rounded leading edge is close to the upper surface near to the apex and progressively moves towards the lower surface with increasing distance from the apex. This situation increases the complexity of the aerodynamics of delta wing aircraft. Several flow phenomena may be observed moving downstream from the wing apex:

1) Laminar flow without flow separation;

2) Laminar flow followed by laminar separation;
3) A laminar separation line moving towards the leading edge followed by laminar flow separation at the leading edge; and
4) Laminar flow at a certain point followed by laminar/turbulent transition.

The complexity of the flow associated with a rounded leading edge has been discussed by Hummel [22-8], Luckring [[22-7], [22-9]] and Schröder et al. [22-10]. For such a case, the onset of the primary separation now depends on the angle of attack, the Reynolds number, the Mach number and the leading edge bluntness itself. The effect of angle of attack and Reynolds number will be addressed later on in this paper.

A particularly interesting feature of the rounded leading edge is the emergence, at moderate angles of attack, of a small suction peak lying inboard of the primary suction peak and originating near the half chord location. This feature has been discussed extensively by Hummel [22-8] and is indicative of an inner vortex with the same sign as the primary vortex. The occurrence of this inner vortex is related to separation near the apex where the relative thickness of the wing is high. Moving down the leading edge, the flow progressively experiences a relatively sharper leading edge and so separation moves back from the upper surface towards the leading edge itself. As it does so, the vorticity from this separation is channelled into a conventional primary vortex that originates further downstream than the inner vortex. With increasing angle of attack, more vorticity is fed into the primary vortex and the inner vortex becomes steadily weaker and finally disappears or merges with the primary vortex somewhere near the trailing edge.

22.4 RESULTS

It should be noted that the results presented in the following sections have not yet been corrected for wind tunnel wall interference effects. The main effect of such a correction would be to change the effective angle of attack of the wing.

22.4.1 Flow Visualization Results

Oil flow patterns on wing configurations develop with time. In the sections that follow, single oil flow images will be presented for each case to highlight the salient flow features. In fact, however, several images were recorded for each case as the oil flow pattern developed on the wing over time. This information can be important as the collection of oil at specific locations on the surface can, for sensitive flows, alter the flow state. A temporal series of images provides reassurance that this has not, in fact, happened.

As an example of the temporal development of the oil flow pattern on the VFE wing, two cases are presented. Figure 22-6 shows the flow development on the sharp-edged wing at a Reynolds number of 1×10^6 and angle of attack of 13.3°. Figure 22-7 shows the flow development for the medium radius wing at the same Reynolds number and angle of attack. In both cases, there are no changes in the apparent flow topology as regions of concentrated oil gather on the wing, suggesting that the flow behaviour is insensitive to the presence of the oil.

Figure 22-6: The Development of the Oil Flow for the Sharp-Edged Wing, R_{mac} = 1 x 10^6 and α = 13.3°.

Figure 22-7: The Development of the Oil Flow for the Medium Radius Wing, R_{mac} = 1 x 10^6 and α = 13.3°.

22.4.1.1 Sharp Leading Edge Wing

Figure 22-8 shows the flow visualizations obtained at a Reynolds number of 2 x 10^6 and at three angles of attack, 13.3°, 18.5° and 23°. In all three cases, the flow patterns exhibit the footprint of a classical delta wing leading edge vortex system. Flow separation takes place at the leading edge and this separation creates the vortex system above the wing. It may be observed that at all three angles of attack the vortex system originates near the apex of the wing and persists to the trailing edge. In the images, the secondary separation line clearly delineates the primary and secondary vortex core locations. In the image corresponding to 23° angle of attack, there is evidence of a loss in coherence of the flow structures near the trailing edge. Presumably, this is indicative of the progression of vortex breakdown over the trailing edge.

(a) (b) (c)

Figure 22-8: Flow Visualization Images for the Sharp Edge Configuration at R_{mac} = 2 x 10^6 and Angles of Attack (a) 13.3°, (b) 18.5° and (c) 23°.

22.4.1.2 Medium Radius Leading Edge Wing

The most direct way to illustrate the effect of rounding the wing leading edges is to compare the flow visualization images from the sharp-edged cases with those obtained on the configuration with the medium radius edges. Figure 22-9 illustrates one such comparison for the 13.3° case at 2 x 10^6 Reynolds number. The first obvious feature of the figure is that the primary vortex structure on the round-edged wing no longer begins at the apex. In fact, it appears to have its origins at about 30% of the root chord down the leading edge. In addition, there is now clear evidence of an additional structure on the inboard sections of the wing. This structure appears to originate near the apex and is likely to be the inboard vortex suggested by Hummel. It has been suggested that this structure will progressively weaken in relation to the primary vortex as the angle of attack of the wing is increased. This is explored in Figure 10 where results are presented for 13.3°, 18.5° and 23°.

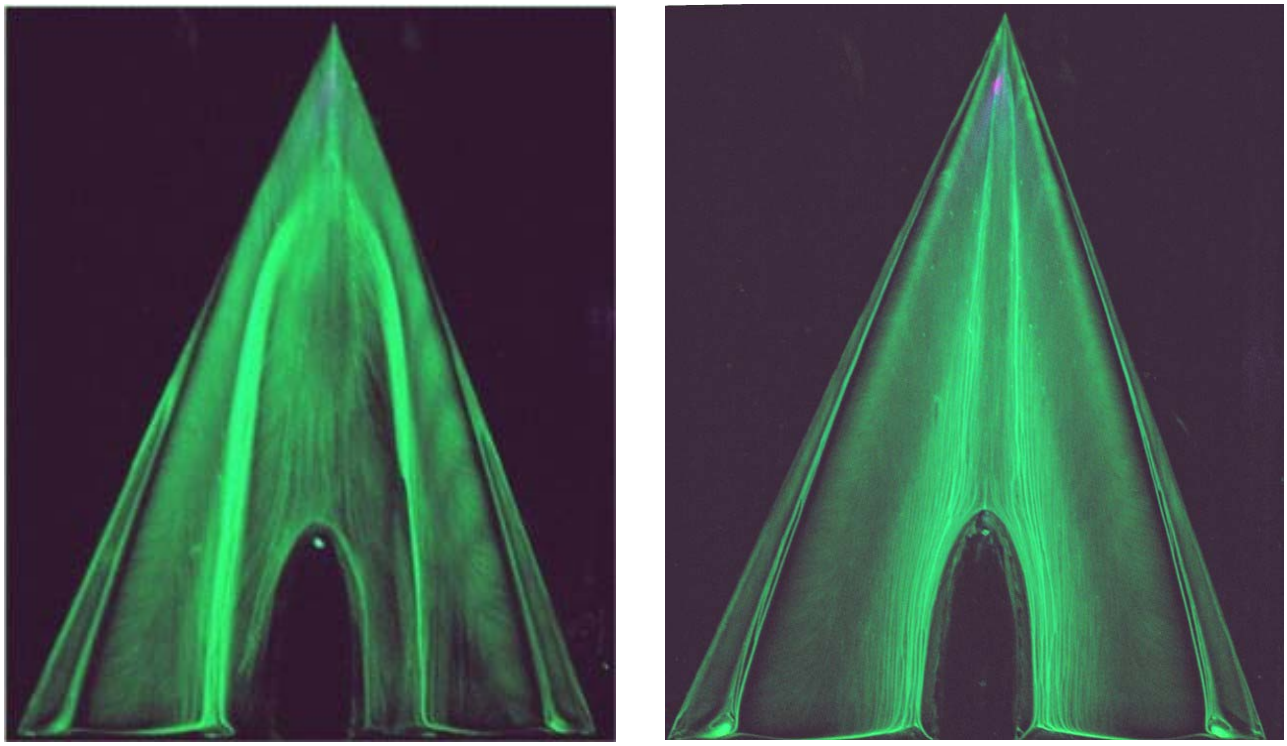

(a) (b)

Figure 22-9: Comparison of Oil Flow Patterns for (a) Rounded and (b) Sharp Leading Edge Configurations at $R_{mac} = 2 \times 10^6$, $\alpha = 13.3°$.

An obvious feature of the results presented in Figure 22-10 is the progressive movement of the origin of the primary vortex from the 30% of root chord location towards the apex as the angle of attack increases from 13.3° up to 23°. At the same time, the inboard structure becomes less distinct and the images begin to resemble more closely those of the sharp leading edges. By 23° there is still a difference between the images for the sharp and medium radius edges suggesting that the flow on inboard sections of the wing differs in the two cases. This may be due to persistence of a weak inboard vortex structure but this cannot be confirmed without flowfield data.

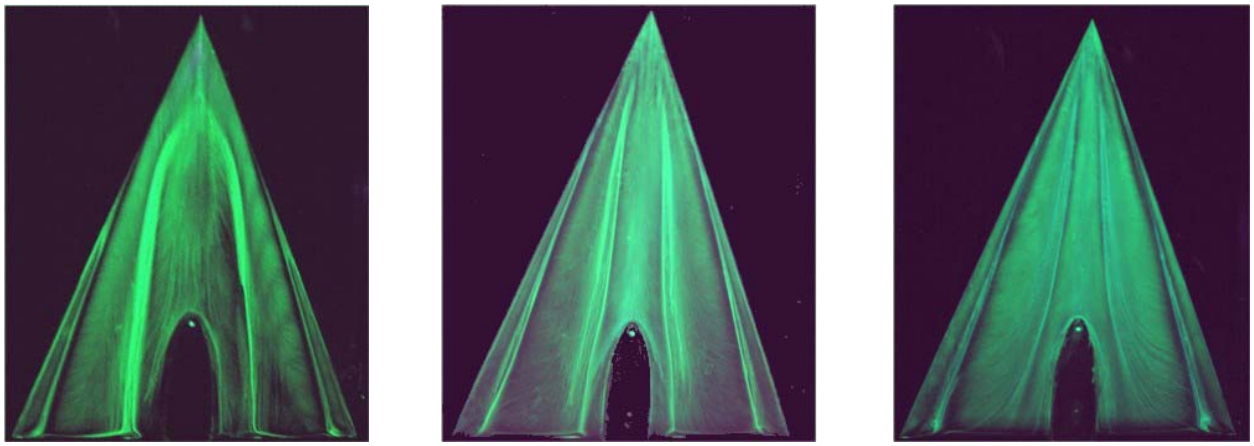

(a) (b) (c)

Figure 22-10: Flow Visualization Images for the Rounded Edge Configuration at R_{mac} = 2 x 10^6 and Angles of Attack (a) 13.3°, (b) 18.5° and (c) 23°.

22.4.1.3 Influence of Reynolds Number on Rounded Leading Edge Flow

The sensitivity of the flow on a sharp edged delta wing to Reynolds number effects is restricted by the fact that separation is effectively forced at the sharp leading edges. For this reason, the Reynolds number has more of an influence on secondary separation rather than the primary separation and it principally alters the relative placement and size of the primary and secondary vortex systems. It has been shown to have almost no effect on the measured lift. On a wing with rounded leading edges, the boundary layer can persist beyond the leading edge before separating on the upper surface of the wing. This is particularly the case near the apex where the relative thickness of the wing is greater. The effect of this delay in separation has been discussed above in relation to the formation of the complex vortex system above the delta wing with the medium radius edges.

The influence of Reynolds number on this process can be observed in Figure 22-11. This figure shows surface oil flow visualizations for Reynolds numbers of 1 x 10^6 and 2 x 10^6 at an angle of attack of 13.3°. The characteristics of the flow pattern at Re = 2 x 10^6 have already been described and, although the flow pattern at 1 x 10^6 looks very similar, there are some important differences. At first glance it appears that the primary vortex structure may extend all the way to the apex for the Re = 1 x 10^6. Indeed the flow pattern in the vicinity of the leading edge looks very similar to that of the sharp-edged wing. The flow pattern further inboard, however, is very similar to that on the medium radius wing suggesting that the inner vortex structure still exists for this case. Closer examination of the leading edge region shows a distinct bend in the dark radial line associated with the primary vortex at about 20 – 30% of root chord. It is not clear that the continuation of this line towards the apex is part of the primary vortex. It is likely that laminar separation is initiated at the leading edge at this low Reynolds number right up to the apex. It may be that the shear layer then undergoes transition and reattaches close to the leading edge, leaving the footprint of a laminar separation bubble. The flow then subsequently behaves in a similar manner to the Re = 2 x 10^6 case.

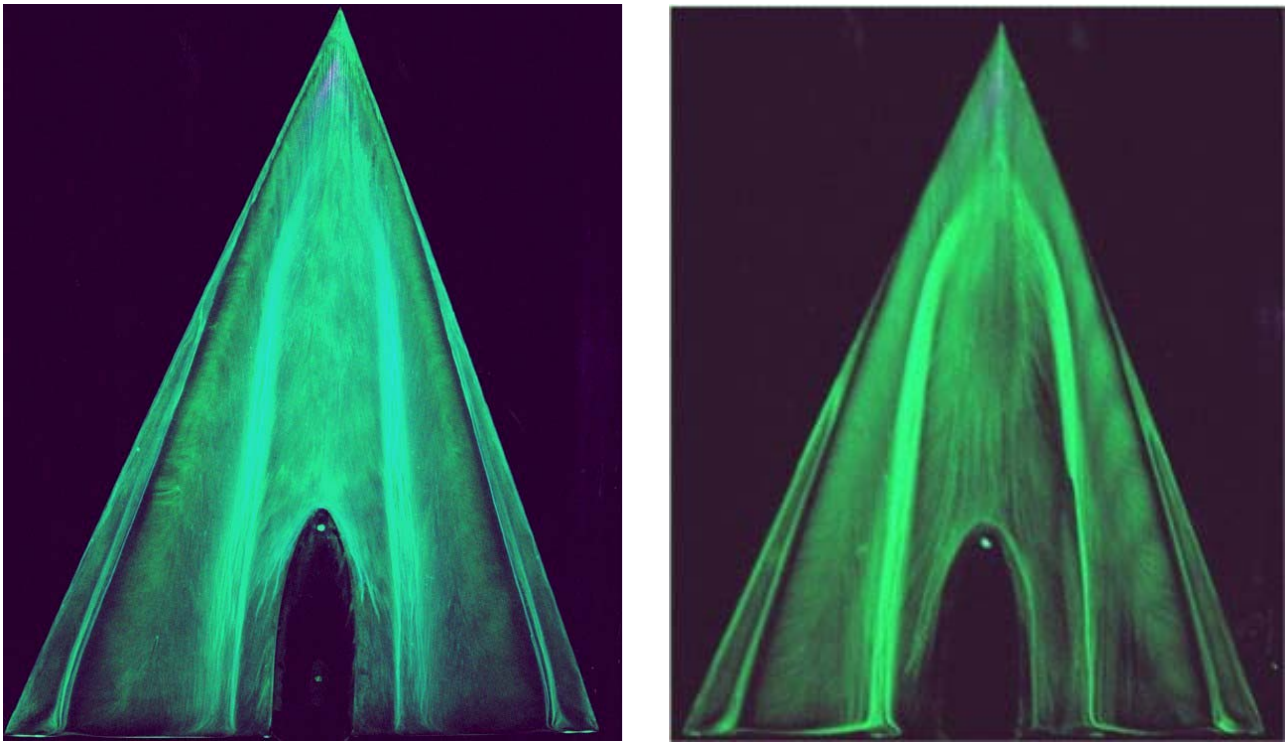

(a) (b)

Figure 22-11: Comparison of Oil Flow Patterns for the Round Edged Configuration at (a) Re = 1 x 10^6 and (b) R_{mac} = 2 x 10^6, α = 13.3°.

At higher angles of attack, separation becomes restricted to the leading edge and the flow patterns at both Reynolds numbers become essentially identical.

22.4.1.4 Further Insight into Leading Edge Rounding

As mentioned previously, four sets of leading edges were manufactured at Glasgow to replicate the original leading edge geometries studied by Chu and Luckring. Although the work reported here focuses on the sharp and medium radius leading edge geometries, some insight into the effect of leading edge rounding can be gained by looking at results from the other cases. As an example, Figure 22-12 compares the flow over the sharp, medium and large radius wings at a Reynolds number of 2 x 10^6 and an angle of attack of 13.3°.

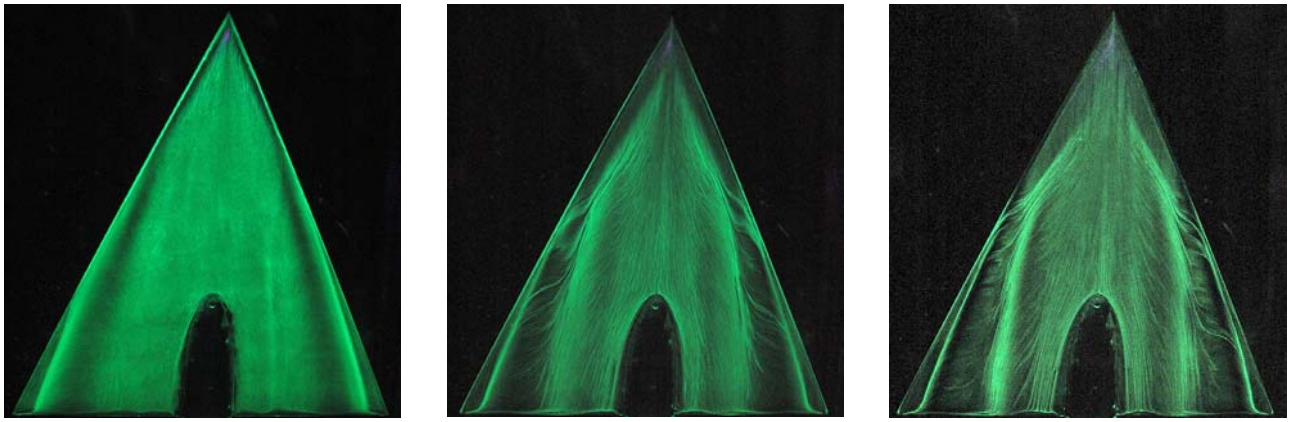

Figure 22-12: The Development of the Primary Vortex for the Large-Edged, R_{mac} = 2 x 10^6 and α = 13.3°.

In this figure, the leading edge vortex structure is clearly not present over the nose portion of the large radius wing. Instead, the flow appears to be initially attached in this region (with a possible leading edge separation bubble very close to the leading edge) and the oil moves in the freestream direction. There is then a separation front which starts some distance downstream of the apex and sweeps out towards the leading edge. The primary vortex system has its origins just upstream of where the separation front meets the leading edge. This case illustrates the fundamentally different flow structures that exist at the leading edge near the apex and further downstream. This is consistent with the observations made earlier in relation to flow structures on the medium radius wing.

22.4.2 Forces and Moments

22.4.2.1 Steady Forces and Moments

In this section data will be presented for all three cases discussed above, i.e. medium edges 1 x 10^6 and 2 x 10^6 and sharp edges 2 x 10^6. The normal force coefficient variations measured on the wing are presented in Figure 22-13. There is a clear Reynolds number effect at the lower angles of attack for the wing with the rounded edges. Initially, the normal force coefficient is higher at the lower Reynolds number. The reasons for this are not immediately obvious but are likely to be associated with the leading edge separation and the effect this has on the strength of the primary vortex system. This effect disappears at about 20° angle of attack in a manner consistent with the trend shown in the surface oil flow visualization, i.e. the flow patterns become identical at the higher angles of attack. Examination of the results for the sharp edged wing would tend to confirm this hypothesis since they have a very similar magnitude and gradient to the results at 1 x 10^6 for the round-edged wing.

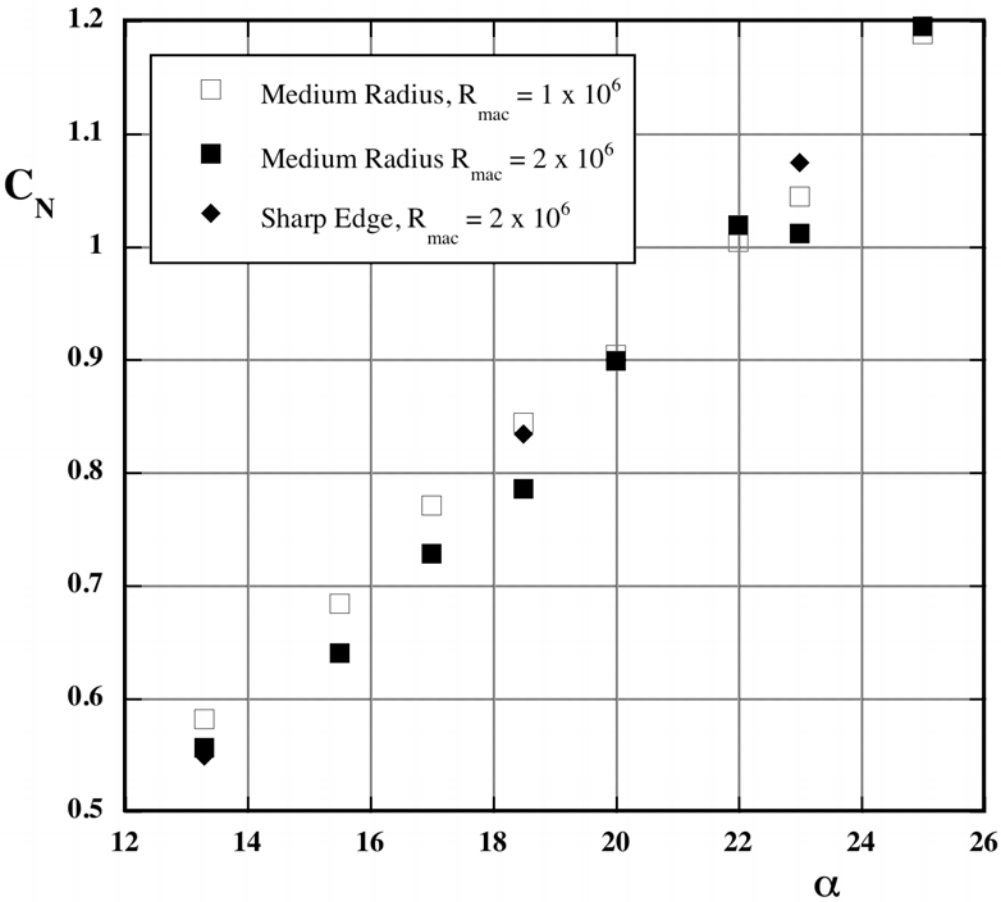

Figure 22-13: Comparison of Normal Force Coefficients for the Three Test Cases.

The measured axial force coefficients are presented in Figure 22-14. It is important to note there that the positive direction is defined as being in the direction of the airflow. The figure shows that although there are slight differences between the data sets for the two leading edge geometries at the same Reynolds number, the main effect visible in the data is the difference between two Reynolds numbers. The axial force coefficient is always higher for the R_{mac} = 1 x 10^6 case and the curve with increasing incidence has a steeper gradient. This is consistent with a larger wake structure at lower Reynolds number that progressively increases as the angle of attack is increased.

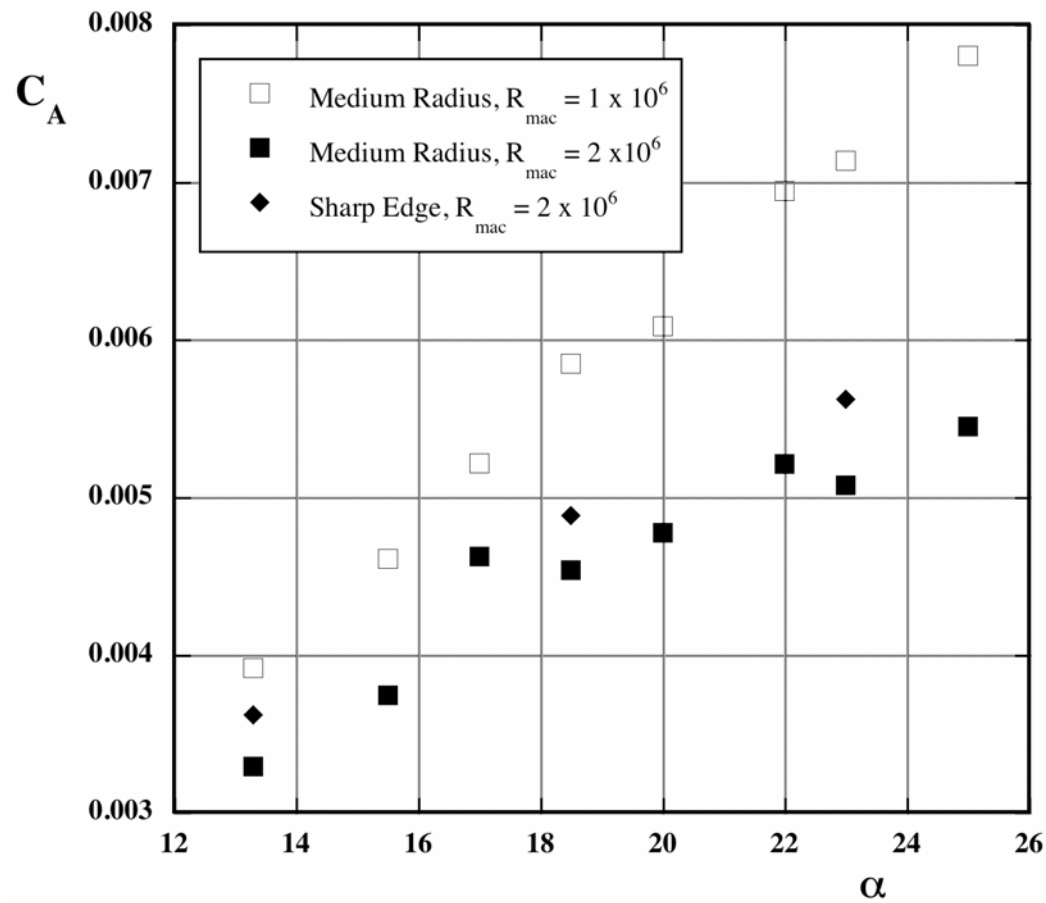

Figure 22-14: Comparison of Axial Force Coefficients for the Three Test Cases.

The final figure in this section, Figure 22-15, shows the pitching moment coefficient measured about the aerodynamic centre. At the lower incidence values, the rounded-edged wing exhibits lower nose down pitching moment values than the sharp-edged wing. In addition, the results for the round-edged wing appear to be relatively insensitive to Reynolds number below approximately 19°. At higher angles of attack, round-edged wing produces larger nose down pitching moments at the lower Reynolds number, achieving similar magnitudes to the sharp-edged wing at 2 x 10^6. The reason for this is not obvious at this stage.

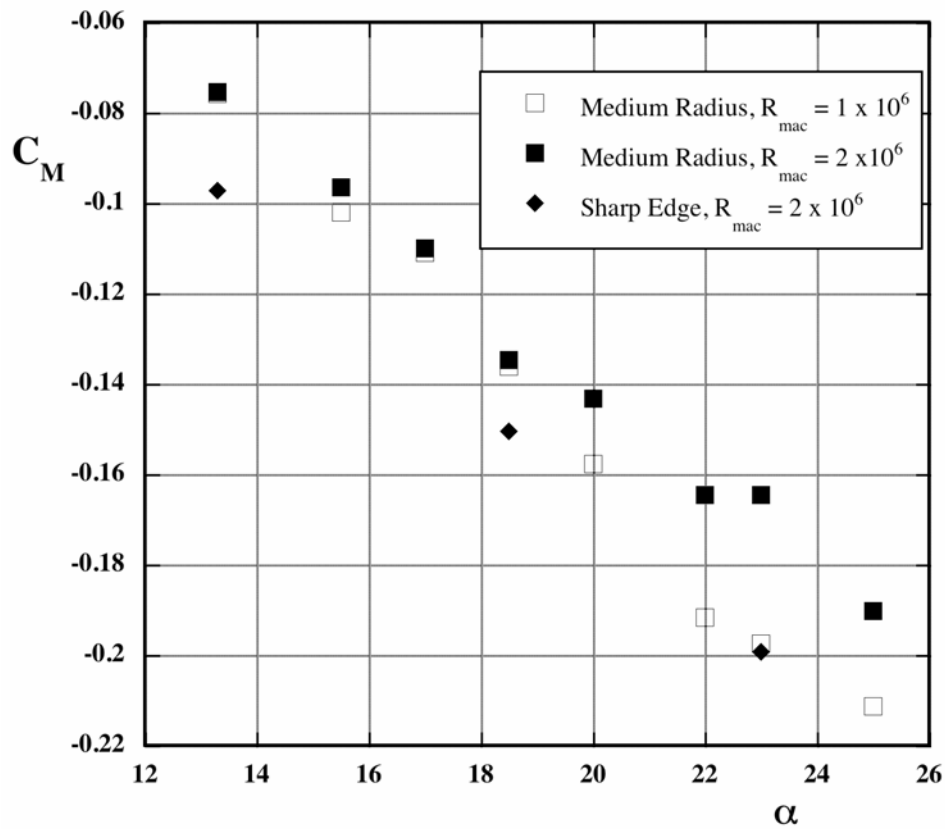

Figure 22-15: Comparison of Pitching Moment Coefficients for the Three Test Cases.

22.5 CONCLUSIONS

Flow visualization and load data have been presented for a 65° delta wing with rounded and sharp leading edges. The data have identified that, as may be expected, the flow topology and the resulting loads become sensitive to Reynolds number when the leading edges are rounded. At higher angles of attack, this sensitivity seems to diminish somewhat but the Reynolds number still influences the pitching moment and tangential force. Unsteady forces were measured but these have not yet been fully analysed. Sample datasets of time varying forces and moments are provided in Appendix 3.5.

Further testing is planned during 2008 to supplement the current measurements. This will include PIV measurement of the flowfield, unsteady surface pressure measurements and infra-red thermography studies of the boundary layer state.

Sample datasets from all the tests described in this chapter are provided in Appendix 3.5.

22.6 REFERENCES

[22-1] Chu, J. and Luckring, J.M.: *Experimental Surface Pressure Data Obtained on 65° Delta Wing Across Reynolds Number and Mach Number Ranges*, NASA TM 4645, 1996.

[22-2] Gad-El-Hak, M. and Blackwelder, R.F.: *The Discrete Vortices from a Delta Wing*, AIAA Journal, Vol. 23, 1985, pp. 961-962.

[22-3] Payne, F.M., Ng, T.T. and Nelson, R.C.: *Experimental Study of the Velocity on a Delta Wing*, 19th AIAA Fluid Dynamics, Plasma Dynamics and Lasers Conference, Honolulu, 1987.

[22-4] Délery, J.M., Legendre, R. and Werlé, H.: *Toward the Elucidation of Three Dimensional Separation*, Annual Review of Fluid Mechanics, Vol. 33, 2001, pp. 129-154.

[22-5] Gursul, I.: *Recent Developments in Delta Wing Aerodynamics*, The Aeronautical Journal, Vol. 108, No. 1087, 2004, pp. 437-452.

[22-6] Renac, F., Barberis, D. and Molton, P.: *Control of Vortical Flow Over a Rounded Leading-Edge Delta Wing*, AIAA Journal, Vol. 43, No. 7, 2005, pp. 1409-1417.

[22-7] Luckring, J.M.: *Reynolds Number and Leading-Edge Bluntness Effects on a 65° Delta Wing*, 40th AIAA Aerospace Sciences Meeting and Exhibit, Reno, 2002.

[22-8] Hummel, D.: *The Second International Vortex Flow Experiment (VFE-2): Objectives and First Results*, Proceedings of IMechE Part G: Journal of Aerospace Engineering, Vol. 220, No. 6, 2006, pp. 559-568.

[22-9] Luckring, J.M.: *Reynolds Number, Compressibility, and Leading Edge Bluntness Effects on Delta Wing Aerodynamics*, 24th International Congress of the Aeronautical Sciences, Yokohama, 2004.

[22-10] Schröder, A., Agocs, J., Frahnert, H., Otter, D., Mattner, H., Kompenhans, J. and Konrath, K.: *Application of Stereo PIV to the VFE-2 65° Delta Wing Configuration at Sub-and Transonic Speeds*, 24th AIAA Applied Aerodynamics Conference, San Francisco, 2006.